

# 2D Magnetic Mesocrystals for Bit Patterned Media

Shanshan Guo, Feng Xu, Baomin Wang,\* Ning Wang, Huali Yang, Pravarthana Dhanapal, Fei Xue,\* Junling Wang, and Run-Wei Li\*

**Bit patterned media exhibits great potential in satisfying the increasing demand for higher information storage density, but the present media fabrication technique is complicated. Here, a 2D magnetic mesocrystal with monodisperse  $\text{CoFe}_2\text{O}_4$  (CFO) nanocrystals is fabricated through a combination of nanoseeds layer growth and oxides self-assembly method. The monodisperse CFO nanomagnets protrude from the substrate surface with perfect crystal facets, specific crystallographic orientation, and are fully relaxed. Systematic magnetic characterizations, such as dynamic cantilever magnetometry for single CFO nanocrystal, magnetic force microscopy, and superconducting quantum interference device magnetometry for large area, reveal the novel tilted magnetic anisotropy and the switchable single domain state. This work provides a new way to fabricate bit patterned media with controlled material structure simply by a nanoseeds-mediated self-assembly method.**

The increasing demand for hard drives with higher storage density has motivated a technology shift from continuous magnetic media to bit patterned media (BPM),<sup>[1]</sup> in which one single bit of information is stored in an individual nanostructure.<sup>[2]</sup> At the present research and development stage, BPM is fabricated using a combination implementation of e-beam lithography, template fabrication, nanoimprint, and magnetic film evaporation,<sup>[1a,3]</sup> and these isolated islands on BPM exhibit polycrystal structure. However, these polycrystal islands suffer from nonuniform microstructure, which inevitably results in variation of magnetic anisotropy among islands, which in turn leads to wide variation of switching field that affects the addressability of individual predefined bits and may cause overwriting of adjacent bits.<sup>[4]</sup> Recently, a unique crystallographically hierarchical structure, which is made up of isolated well-organized

nanocrystals, named mesocrystal, has been synthesized by a one-step self-assembly crystallization process.<sup>[5]</sup> Through this novel self-assembly process, magnetic mesocrystals composed of discrete magnetic nanocrystals embedded in an immiscible nonmagnetic matrix have been achieved.<sup>[6]</sup> However, the embedded nanomagnets inevitably suffer from mismatch strain and defects at the interfaces of two mixed phases,<sup>[7]</sup> which may produce uncontrollable magnetic property for each nanomagnet and contribute to wide variation of switching field. Thus, magnetic mesocrystals composed of monodisperse well-organized nanocrystals that are not embedded in a matrix have great potential in BPM. Here, we report


the fabrication of 2D magnetic  $\text{CoFe}_2\text{O}_4$  (CFO) mesocrystal through a combination of nanoseeds layer growth and oxides self-assembly method. The monodisperse CFO nanomagnets protrude from the substrate surface with perfect crystal facets, specific crystallographic orientation, and are fully relaxed. Systematic magnetic characterizations, such as dynamic cantilever magnetometry (DCM) for single CFO nanocrystal, magnetic force microscopy (MFM), and superconducting quantum interference device (SQUID) magnetometer for large area, reveal the novel tilted magnetic anisotropy and the switchable single domain state.

A schematic description of the fabrication process is shown in **Figure 1a**. The nanoseeds layer is prepared based on the different surface energy anisotropy of perovskites and spinels. Most perovskites are characterized by low-energy {100}

S. Guo, Prof. B. Wang, Dr. H. Yang, Dr. P. Dhanapal, Prof. R.-W. Li  
CAS Key Laboratory of Magnetic Materials and Devices  
Ningbo Institute of Materials Technology and Engineering  
Chinese Academy of Sciences  
Ningbo 315201, P. R. China  
E-mail: wangbaomin@nimte.ac.cn; runweili@nimte.ac.cn

S. Guo, Prof. B. Wang, Dr. H. Yang, Dr. P. Dhanapal, Prof. R.-W. Li  
Zhejiang Province Key Laboratory of Magnetic Materials  
and Application Technology  
Ningbo Institute of Materials Technology and Engineering  
Chinese Academy of Sciences  
Ningbo 315201, P. R. China

S. Guo  
University of Chinese Academy of Sciences  
Beijing 100049, P. R. China

 The ORCID identification number(s) for the author(s) of this article can be found under <https://doi.org/10.1002/admi.201800997>.

DOI: 10.1002/admi.201800997

F. Xu, Dr. N. Wang, Prof. F. Xue  
Anhui Province Key Laboratory of Condensed Matter  
Physics at Extreme Conditions  
High Magnetic Field Laboratory  
Chinese Academy of Sciences  
Hefei 230031, P. R. China  
E-mail: xuef@hmfll.ac.cn

F. Xu, Dr. N. Wang, Prof. F. Xue  
Collaborative Innovation Center of Advanced Microstructures  
Nanjing University  
Nanjing 210093, P. R. China

F. Xu  
University of Science and Technology of China  
Hefei 230026, P. R. China

Prof. J. Wang  
School of Materials Science and Engineering  
Nanyang Technological University  
Singapore 639798, Singapore

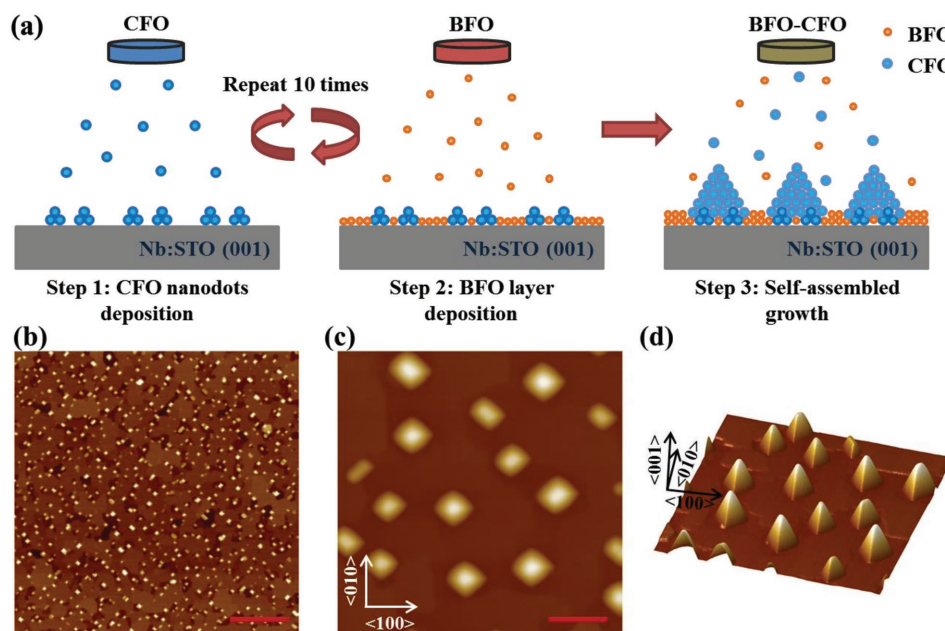


**Figure 1.** CFO mesocrystal fabrication process. a) Schematic flowchart of the CFO mesocrystals fabrication. b) Topography image of the CFO nanoseeds layer. c,d) Topography image of the as-grown CFO mesocrystal in 2D and 3D view. The scale bar in (b) and (c) is 200 nm.

surfaces.<sup>[8]</sup> On the other hand, in spinels, the {111} surface typically has the lowest surface energy.<sup>[9]</sup> The growth mode of perovskite and spinel phases can, therefore, be very different when they are deposited on a substrate surface. Here, (001) oriented perovskite Nb-doped  $\text{SrTiO}_3$  (Nb:STO) is chosen as the substrate. The nanoseeds are deposited by pulsed laser deposition using a CFO and  $\text{BiFeO}_3$  (BFO) dual-target setup. The laser first ablates the CFO target, and the spinel CFO wets the substrate partially, leading to the formation of islands, as illustrated in step 1. The laser ablates the BFO target. Because of the good structure compatibility with Nb:STO, perovskite BFO tends to follow a layer-by-layer growth mode as shown in step 2 and contributes to stabilize and separate the CFO nanoislands. We repeat the deposition of CFO and BFO cycles ten times to ensure that the CFO nanoislands are large enough to act as the nucleating points. Each cycle is well controlled so that neither CFO nor BFO form one continuous layer to avoid the formation of a multilayered structure. Surface morphology of the nanoseeds layer was probed by atomic force microscopy (AFM), which reveals  $\approx 10$  nm monodisperse nanodots uniformly distributed on the surface as shown in Figure 1b. Finally, the self-assembly process, which occurs specifically for immiscible materials, follows by ablation of a BFO-CFO composite target,<sup>[6a]</sup> as illustrated by step 3. The nanoseeds layer induces further growth of CFO at certain locations, leading to particles with a lateral size of 100 nm dispersed homogeneously on the substrate, as shown in Figure 1c. From the 3D view (Figure 1d), we can see that these monodispersed particles protrude from the surface and exhibit a pyramid-like structure with specific crystallographic orientation. The ridges of the nanopyramids align along  $\langle 100 \rangle$  and  $\langle 010 \rangle$  directions. The nanoseeds layer is essential to achieve this well-organized 2D CFO mesocrystal (Figure S1a, Supporting Information). Besides, the size of the nanopyramids can be modulated with

great flexibility by increasing/decreasing the deposition time (Figure S2, Supporting Information). The CFO ordered arrays can be fabricated through the nanoseeds layer mediated oxides self-assembly method on a prepatterned substrate (Figure S3, Supporting Information).

Transmission electron microscopy (TEM) analyses were conducted on the as-grown sample from planar view. Bright-field (BF) TEM image resolves the system to be pyramid-like particles dispersed on a flat layer (Figure 2a), and the corresponding Co elemental mapping further confirms the CFO phase in the nanocomposite system, as Co appears only in the nanopyramids (Figure 2b). X-ray ( $\theta$ - $2\theta$ ) scan shown in Figure 2c reveals the good crystallinity and epitaxial quality of the nanostructure, as reflected by the diffraction peaks from (00l)-oriented spinel CFO, perovskite BFO, and Nb:STO substrate, respectively. The  $c$ -axis lattice parameter of the CFO is calculated as 8.38 Å, suggesting that it is fully relaxed. The epitaxial structure was further confirmed by the in-plane  $\phi$ -scans, as shown in Figure 2d. The fourfold symmetry and the cubic-to-cubic correlation of both constituents and single-crystal Nb:STO substrate indicate a structure-coupled epitaxial growth.

To further investigate the microstructures of the CFO nanopyramids, we conducted cross-sectional TEM, as shown in Figure 3. It is worth to note that all of the CFO phase (indicated by arrows in Figure 3a) form facets and protrude from the substrate surface, with an average height of 60 nm. It is totally different from the BFO-CFO nanocomposite fabricated by oxide self-assembly without a seeds layer (Figure S1b, Supporting Information). Energy-dispersive X-ray spectroscopy (EDS) mapping identifies chemically the individual (well-aligned) pyramid as CFO (Figure 3b). Moreover, Figure 3a,b confirms the non-embedding nature of the CFO nanopyramids. Notably, there is a thin BFO layer beneath the CFO nanopyramids which can be seen from the Bi element mapping. This thin BFO layer is

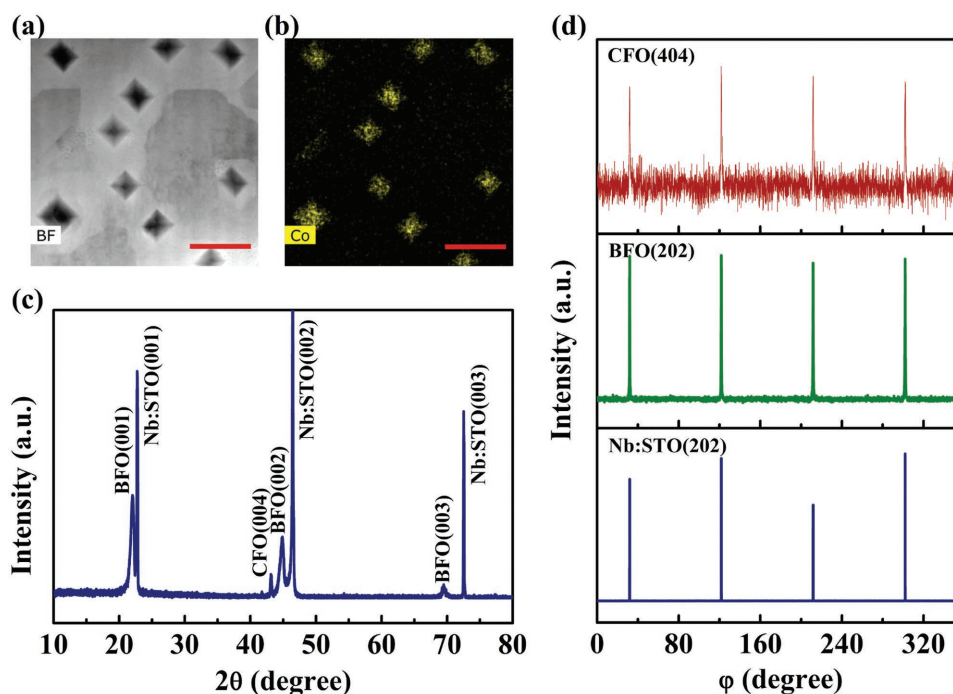


**Figure 2.** Phase and epitaxial growth of CFO mesocrystals. a) In-plane BF-TEM image of CFO mesocrystals, and b) the corresponding same region Co elemental mapping. Scale bar, 200 nm. c) X-ray ( $\theta$ - $2\theta$ ) scan of CFO mesocrystal showing only (00l) type peaks, corresponding to CFO, BFO, and Nb:STO substrate. d) A fourfold symmetry and epitaxial correlations between CFO, BFO, and single-crystal substrate revealed by  $\phi$ -scans.

generated during the seeds layer growth (Figure 1a). To extract atomic-scale information, Figure 3d exhibits the zoom-in high-resolution TEM (HRTEM) image of the marked area in Figure 3c. The HRTEM image shown in Figure 3d confirms the {111}-type facets, which has the lowest surface energy for the spinels, of the CFO nanopyramids. In addition, one can see that there is a transition region between CFO nanopyramids and Nb:STO substrate. These findings are also corroborated by cross-sectional EDS mapping, where a thin Bi-rich layer can be identified (Figure 3b).

For BPM, one bit of information is stored in a single magnetic nanoisland. So it is imperative to understand the intrinsic magnetic properties of the single nanoisland. However, due to the weak magnetic response of a nanometer-scale unit, such information is difficult to obtain by conventional instruments. In the present study, we investigate the magnetic properties of an individual CFO nanopyramid using the DCM, which is an effective method for the study of nanomagnetic materials.<sup>[10]</sup> DCM measures the shift of the cantilever's resonance frequency caused by the torque acting on a nanomagnet at the tip of cantilever from a magnetic field. By using an ultra-soft, single-crystal Si cantilever, a sufficiently high sensitivity can be achieved. Individual CFO nanopyramid is obtained by focused ion beam (FIB) and mounted onto the cantilever with Pt as adhesive using FEI Helios Nanolab 600i. The experiment setup is schematically shown in Figure 4a. Detail information about the cantilever and test specimen is shown in Figure S4 (Supporting Information).

DCM experiments are carried out in a vacuum chamber with a pressure below  $1 \times 10^{-6}$  mbar in the cryostat. A vector superconducting magnet produces a magnetic field up to 90 kOe

along  $z$ -axis, and 10 kOe along  $x$  and  $y$ -axes. The changing of cantilever's resonant frequency is recorded while the magnetic field is swept. At large fields, the frequency shift can be modeled by employing a Stoner–Wohlfarth (S–W) uniformly magnetized particle approximation, given in SI units

$$\frac{\Delta f}{f_0} = \frac{\mu_0 m_s H H_k}{2kl_e^2(H + H_k)} \quad (1)$$

where  $f_0$  is the cantilever's resonance frequency at zero field,  $m_s$  is the saturation magnetic moment of the sample,  $k$  is the cantilever's spring constant, and  $l_e$  is the effective length of cantilever, which is related to the bending mode ( $l_e = 0.75l_0 - 0.85l_0$ ). And  $H_k = 2K_u/M_s$  is the effective uniaxial anisotropy field.  $K_u$  is uniaxial anisotropy and  $M_s$  is saturation magnetization. We measure  $f_0$  as a function of  $H$  with an oscillation amplitude of  $x \approx 100$  nm ( $x \ll l_e$ ).

The magnetic signal from the CFO nanopyramid is very small. A reference experiment was first conducted to confirm that the Pt and the substrate have negligible effect on the frequency shift of the cantilever, as shown in Figure S5 (Supporting Information). The experiments were carried out for CFO nanopyramid in three orientations as illustrated in the insets of Figure 4. The measured frequency shift is plotted with respect to the applied magnetic field. The dependence of  $\Delta f$  versus  $H$  is fundamentally different for each orientation, so the magnetic anisotropy can be acquired. Figure 4b shows  $\Delta f$  versus  $H$  along  $Z$  axis, where  $\Delta f$  is positive for large  $|H|$  and approaches a constant value. At low fields, the data show a clear hysteresis and a superposition at about 7 kOe. With the S–W assumption, the superposition in hysteresis loop indicates the



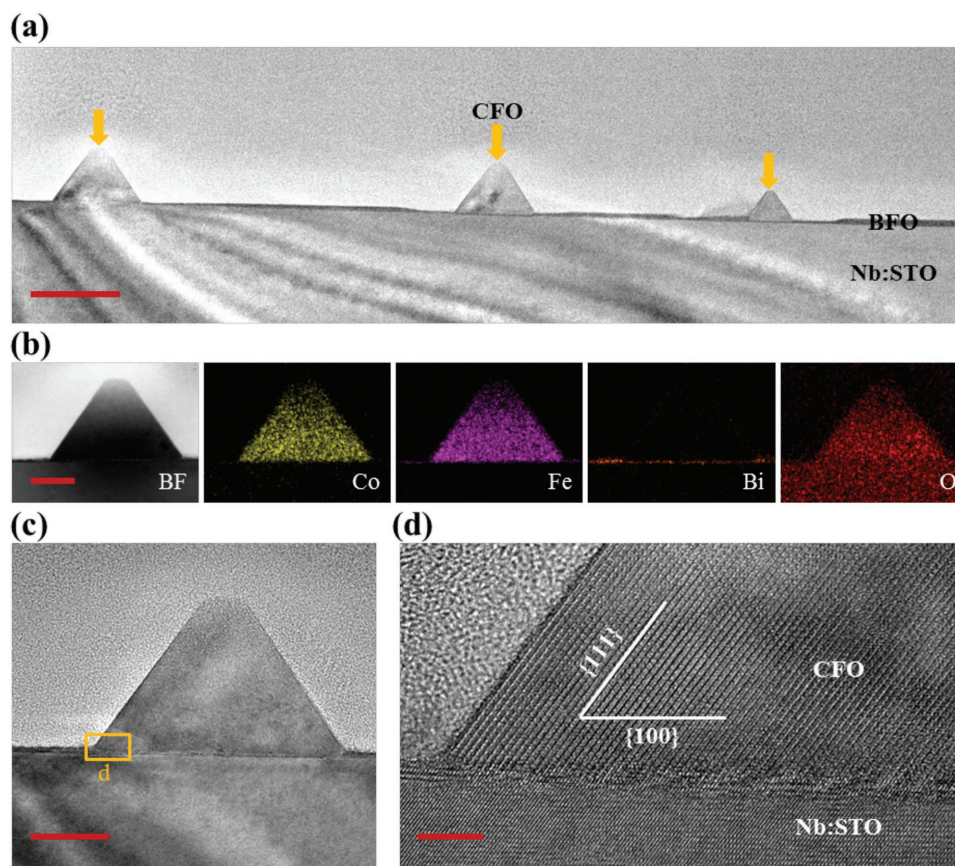


**Figure 3.** High-resolution structural and chemical analysis of CFO mesocrystals. a) A typical cross-sectional TEM image of the CFO mesocrystals. The CFO phase is indicated by orange arrows. Scale bar, 100 nm. b) The TEM image of the sample and the corresponding same region EDS mapping of the Co, Fe, Bi, and O from left to right, respectively. Scale bar, 30 nm. c) Cross-sectional TEM image of one CFO nanopyramid. Scale bar, 30 nm. d) High-resolution cross-sectional TEM image of the area marked in (c) viewed from zone axis  $[1-10]$ . The crystallographic axis in-plane of the pyramid is indicated. Scale bar, 5 nm.

saturation magnetization. So we can conclude that the saturation magnetization field of the CFO nanopyramid is about 7 kOe, which is similar to that obtained from the macroscopic  $M-H$  data (see Figure 4e). In the other configurations, the  $\Delta f$  versus  $H$  curves are more complex. In Figure 4c,  $\Delta f$  versus  $H$  along  $y$ -axis becomes negative, and eventually approaches zero at large  $|H|$ , and two curves coincide well. The minima in  $\Delta f$  are observed near +6.5 and -6.5 kOe. In Figure 4d,  $\Delta f$  versus  $H$  perpendicular to the oblique plane of the CFO nanopyramid shows hysteresis at low fields in a “V-shape” and exhibits a negative slope at high fields. Three different orientations show three different results, so we can conclude that the CFO nanopyramid shows magnetic anisotropy. We have also studied the macroscopic magnetic properties of the CFO mesocrystals using SQUID magnetometry. The magnetic hysteresis loops ( $M-H$  loops) shown in Figure 4e were measured with the magnetic field parallel, perpendicular, and inclined to the substrate surface. The  $M-H$  loop measured with the  $H$  tilted shows the smallest coercivity (0.25 kOe) and the highest rectangle factor, indicating the magnetic easy axis alignment. And anisotropy constant  $K_u$  and anisotropy field  $H_k$  were calculated from the magnetization curves (Figure S6, Supporting Information).  $K_u$  and  $H_k$  of the CFO mesocrystals are  $8.5 \times 10^6$  erg  $\text{cm}^{-3}$  and

17 kOe, respectively. Thus, CFO mesocrystals reported here are suitable for BPM application from the anisotropy field point of view. Details of the calculation and discussions can be found in the Supporting Information.

Microscopic magnetic properties of the CFO mesocrystals were assessed by MFM. Figure 5a shows the MFM phase image of the as-grown sample with the contours of the nanopyramids superimposed, respectively. The inset of Figure 5a is the corresponding topography. In our study, the CoCr-coated magnetic tip was magnetized in an upward direction before measurements. The dark contrast suggests attractive force between the tip and the nanopyramid and the upward magnetization. While the bright contrast, suggesting repulsive force between the tip and the nanopyramid, indicates downward magnetization. As shown in Figure 5c, after applying an out-of-plane magnetic field to saturate the CFO nanopyramids, the remnant states of the nanopyramids show uniform single-domain dark contrast. And they turn to bright contrast after being subjected to an opposite field (Figure 5d), indicating switching of magnetization. The good thermal stability of monodisperse CFO mesocrystal and its magnetic domains was confirmed by temperature dependence of topography and MFM images, which keep stable up to 343 K (Figure S8,

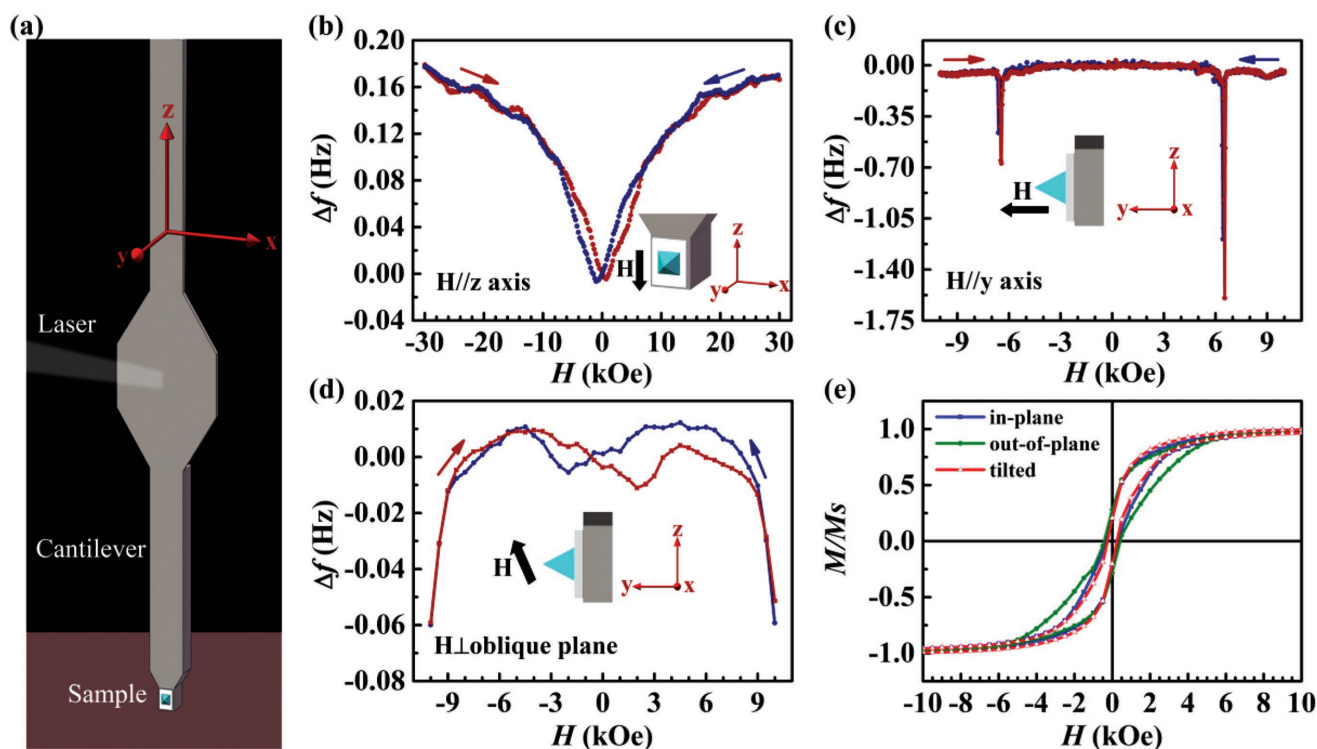


**Figure 4.** DCM characterization of an individual CFO nanopyramid and macroscopic magnetic characterization. a) Schematic diagram of the cantilever magnetometry experimental setup. Resonant frequency shift of the cantilever with an individual CFO nanopyramid as a function of applied magnetic field along the b) pyramid ground plane//z-axis and c) pyramid vertex axis//y-axis, and perpendicular to the d) pyramid lateral face axis. The insets in (b), (c), and (d) are the schematic diagrams of the direction of magnetic field applied with respect to CFO nanopyramid structure. e) Normalized magnetic-hysteresis loops from along in-plane, out-of-plane, and tilted axis to the nanopyramid CFO mesocrystals.

Supporting Information). Furthermore, the Curie temperature ( $T_c$ ) of CFO mesocrystal obtained from the temperature dependence of magnetization ( $M$ - $T$ ) curve is close to that of CFO bulk  $\approx 760$  K<sup>[11]</sup> (Figure S9, Supporting Information), indicating the good thermal stability of CFO mesocrystal. The contrasts at the rim of the pyramids, as shown in Figure 5b–d, may originate from the tilted magnetic anisotropy of the nanopyramids. Considering the structure symmetry, a fourfold magnetic anisotropy axis can be expected. This special magnetic configuration may lead to multistate storage to further improve memory capacity in BPM (Figure S7, Supporting Information). However, further evaluation is limited by the

low resolution of MFM technique and a more precise characterization technique is needed.

In summary, we have developed a new method to fabricate 2D magnetic mesocrystals consisting of monodisperse CFO nanomagnets. The monodisperse CFO nanomagnets are single crystal with uniform pyramid-like shape and specific crystallographic orientation, and fully relaxed. All of these features should play positive roles in eliminating the intrinsic SFD for BPM application. Furthermore, systematic characterizations confirm the switchable single domain state, good thermal stability, and large magnetic anisotropy, which should satisfy the demands of storage medium. The method shows great

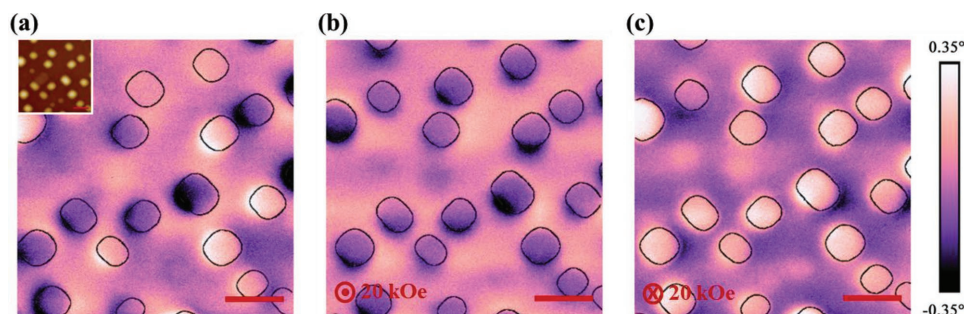


**Figure 5.** Magnetic domain characterization of CFO nanopyramid mesocrystal. The MFM phase scan image of the a) pristine state, after the applied magnetic field of magnitude equal to 20 kOe b) along out-of-plane and c) into the plane of the image shown. The top-left inset in (a) is the corresponding topography of the same area. The CFO nanopyramid magnetic domains are outlined with black color. Scale bar, 200 nm.

flexibility in controlling the island size. Last but not the least, if combined with nanopatterned substrates, ordered nanomagnet arrays can be fabricated. Though much work still needs to be done from application point of view, the technique reported here is definitely of interest for both fundamental study and technology development.

## Experimental Section

**Sample Fabrication:** Multitarget system of bulk CFO, BFO, and BFO-CFO discs was used to fabricate 2D magnetic CFO mesocrystal on an (001) oriented Nb:STO substrate by pulsed laser deposition with a KrF ( $\lambda = 248$  nm) excimer laser. The laser beam was focused on the target with an energy density of  $\approx 1.4$  J cm $^{-2}$ . Samples were deposited at the substrate temperature of 750 °C and in a dynamic oxygen pressure of 200 mTorr. In the growth process of CFO nanoseeds layer, two separate single-phase targets, CFO and BFO, were alternately ablated. Each cycle was well controlled so that neither CFO nor BFO form one continuous layer to avoid the formation of a multilayered structure. Typically, five pulses were incident on the CFO target followed by 30 on the BFO target, which was repeated ten times to form a nanoseeds layer with  $\approx 10$  nm monodisperse CFO nanodots. Then laser beam ablated the BFO-CFO composite target at a frequency of 2 Hz. After the deposition process, samples were cooled to room temperature at 4 °C min $^{-1}$  with 100 Torr O $_2$  to minimize the creation of oxygen vacancies. Patterned dot arrays were written on the (001)-oriented Nb:STO substrate by a Ga focused ion beam of FEI Helios Nanolab 600i dual beam microscope. The acceleration voltage and current were set at 30 kV and 24 pA, respectively. The ion-damaged regions were then etched by a concentrated aqueous solution of HCl for 15 s under ultrasonic agitation. Afterward, the templated substrates were cleaned by acetone under ultrasonic agitation.

**Structure Characterization:** The sample structure was investigated by AFM, high-resolution X-ray diffraction (XRD), and TEM. The specimens of in-plane or cross-sectional TEM analysis were prepared using FIB.

**Magnetic Property Measurements:** The magnetic property of the single CFO nanopillar was detected by DCM. Individual CFO nanopillar was obtained by FIB and mounted onto the cantilever with Pt as adhesive using FEI Helios Nanolab 600i. The detailed preparation process of DCM test specimen is shown in Figure S2 (Supporting Information). Macroscopic magnetic property was studied using SQUID magnetometry with the magnetic field parallel, perpendicular, and inclined to the substrate surface. To acquire the information of magnetic anisotropy, magnetization curves were acquired after the samples were demagnetized by annealing it at 820 K for 15 min. In the temperature-dependent magnetization measurement, the sample was first cooled from 830 to 300 K without a magnetic field, and then sequentially raised to 830 K. The magnetization responses were recorded on the heating cycle with a recording field of 500 Oe. Magnetic domains were detected by MFM. The Co/Cr-coated magnetic tip, which was magnetized along an upward direction in advance, was used to probe the magnetic response of the CFO mesocrystals.

## Supporting Information

Supporting Information is available from the Wiley Online Library or from the author.

## Acknowledgements

This work was supported by the National Key Research and Development Program of China (2016YFA0201102, 2017YFA0303201), the National Natural Science Foundation of China (51571208, 51525103, 11474295,

11374305, 11604338, 6171101158), the Youth Innovation Promotion Association of the Chinese Academy of Sciences (2016270), the Key Research Program of the Chinese Academy of Sciences (KJZD-EW-M05), Ningbo Science and Technology Innovation Team (2015B11001), the Technological Development Grant of Hefei Science Center of Chinese Academy of Sciences (2014TDG-HSC001), and the Major Program of Development Foundation of Hefei Center for Physical Science and Technology (2017FXZY003). F.X. also thanks the support of Recruitment Program for Young Professionals.

## Conflict of Interest

The authors declare no conflict of interest.

## Keywords

2D magnetic CoFe $_2$ O $_4$  mesocrystals, bit patterned media, nanoseeds-mediated self-assembly, single domain state, tilted magnetic anisotropy

Received: July 2, 2018  
Published online:

- [1] a) T. R. Albrecht, H. Arora, V. Ayanoor-Vitikkate, J.-M. Beaujour, D. Bedau, D. Berman, A. L. Bogdanov, Y.-A. Chapuis, J. Cushen, E. E. Dobisz, G. Doerk, H. Gao, M. Grobis, B. Gurney, W. Hanson, O. Hellwig, T. Hirano, P.-O. Jubert, D. Kercher, J. Lille, Z. Liu, C. M. Mate, Y. Obukhov, K. C. Patel, K. Rubin, R. Ruiz, M. Schabes, L. Wan, D. Weller, T.-W. Wu, E. Yang, *IEEE Trans. Magn.* **2015**, 51, 0800342; b) A. Kikitsu, *J. Magn. Magn. Mater.* **2009**, 321, 526; c) D. Weller, H. Brändle, G. Gorman, C.-J. Lin, H. Notarys, *Appl. Phys. Lett.* **1992**, 61, 2726; d) H. J. Richter, *J. Magn. Magn. Mater.* **2009**, 321, 467.
- [2] a) R. L. White, R. M. H. New, R. F. W. Pease, *IEEE Trans. Magn.* **1997**, 33, 990; b) H. J. Richter, A. Y. Dobin, O. Heinonen, K. Z. Gao, R. J. M. v. d. Veerdonk, *IEEE Trans. Magn.* **2006**, 42, 2255.
- [3] a) X. Yang, S. Xiao, K. Lee, D. Kuo, D. Weller, presented at 53rd Annual Conf. Magnetism and Magnetic Materials, Austin, TX, November **2008**; b) D. Kercher, presented at 53rd Annual Conf. Magnetism and Magnetic Materials, Austin, TX, November **2008**.
- [4] a) O. Hellwig, A. Berger, T. Thomson, E. Dobisz, Z. Z. Bandic, H. Yang, D. S. Kercher, E. E. Fullerton, *Appl. Phys. Lett.* **2007**, 90, 162516; b) B. Pfau, C. M. Günther, E. Guehrs, T. Hauet, H. Yang, L. Vinh, X. Xu, D. Yaney, R. Rick, S. Eisebitt, O. Hellwig, *Appl. Phys. Lett.* **2011**, 99, 062502; c) H. Oezelt, A. Kovacs, J. Fischbacher, P. Matthes, E. Kirk, P. Wohlhüter, L. J. Heyderman, M. Albrecht, T. Schrefl, *J. Appl. Phys.* **2016**, 120, 093904; d) J. W. Lau, R. D. McMichael, S. H. Chung, J. O. Rantschler, V. Parekh, D. Litvinov, *Appl. Phys. Lett.* **2008**, 92, 012506.
- [5] a) H. Cölfen, M. Antonietti, *Angew. Chem., Int. Ed.* **2005**, 44, 5576; b) R. Q. Song, H. Cölfen, *Adv. Mater.* **2010**, 22, 1301; c) Y.-Y. Kim, A. S. Schenk, J. Lhli, A. N. Kulak, N. B. J. Hetherington, C. C. Tang, W. W. Schmahl, E. Griesshaber, G. Hyett, F. C. Meldrum, *Nat. Commun.* **2014**, 5, 4341.
- [6] a) H. Zheng, J. Wang, S. E. Lofland, Z. Ma, L. Mohaddes-Ardabili, T. Zhao, L. Salamanca-Riba, S. R. Shinde, S. B. Ogale, F. Bai, D. Viehland, Y. Jia, D. G. Schlom, M. Wuttig, A. Roytburd, R. Ramesh, *Science* **2004**, 303, 661; b) J.-C. Yang, Q. He, Y.-M. Zhu, J.-C. Lin, H.-J. Liu, Y.-H. Hsieh, P.-C. Wu, Y.-L. Chen, S.-F. Lee, Y.-Y. Chin, H.-J. Lin, C.-T. Chen, Q. Zhan, E. Arenholz, Y.-H. Chu, *Nano Lett.* **2014**, 14, 6073; c) H. Zheng, F. Straub, Q. Zhan, P.-L. Yang, W.-K. Hsieh, F. Zavaliche, Y.-H. Chu, U. Dahmen, R. Ramesh, *Adv. Mater.* **2006**, 18, 2747; d) H. Zheng, Q. Zhan,



- F. Zavaliche, M. Sherburne, F. Straub, M. P. Cruz, L.-Q. Chen, U. Dahmen, R. Ramesh, *Nano Lett.* **2006**, 6, 1401; e) N. M. Aimon, H. K. Choi, X. Y. Sun, D. H. Kim, C. A. Ross, *Adv. Mater.* **2014**, 26, 3063; f) S. M. Stratulat, X. Lu, A. Morelli, D. Hesse, W. Erfurth, M. Alexe, *Nano Lett.* **2013**, 13, 3884.
- [7] a) J. L. Macmanus-Driscoll, P. Zerrer, H. Wang, H. Yang, J. Yoon, A. Fouchet, R. Yu, M. G. Blamire, Q. Jia, *Nat. Mater.* **2008**, 7, 314; b) Y.-H. Hsieh, J.-M. Liou, B.-C. Huang, C.-W. Liang, Q. He, Q. Zhan, Y.-P. Chiu, Y.-C. Chen, Y.-H. Chu, *Adv. Mater.* **2012**, 24, 4564.
- [8] a) J. Padilla, D. Vanderbilt, *Phys. Rev. B* **1997**, 56, 1625; b) J. Padilla, D. Vanderbilt, *Surf. Sci.* **1998**, 418, 64; c) B. Meyer, J. Padilla, D. Vanderbilt, *Faraday Discuss.* **1999**, 114, 395; d) T. Sano, D. M. Saylor, G. S. Rohrer, *J. Am. Ceram. Soc.* **2003**, 86, 1933; e) M. Alfredsson, J. P. Brodholt, D. P. Dobson, A. R. Oganov, C. R. A. Catlow, S. C. Parker, G. D. Price, *Phys. Chem. Miner.* **2005**, 31, 671; f) T. Sano, C. S. Kim, G. S. Rohrer, *J. Am. Ceram. Soc.* **2005**, 88, 993.
- [9] a) R. K. Mishra, G. Thomas, *J. Appl. Phys.* **1977**, 48, 4576; b) R. L. Stewart, R. Bradt, *J. Mater. Sci.* **1980**, 15, 67; c) M. R. Huang, C. W. Lin, H. Y. Lu, *Appl. Surf. Sci.* **2001**, 177, 103; d) U. Lüders, F. Sánchez, J. Fontcuberta, *Phys. Rev. B* **2004**, 70, 045403; e) N. J. v. d. Laag, C. M. Fang, G. d. With, G. A. d. Wijs, H. H. Brongersma, *J. Am. Ceram. Soc.* **2005**, 88, 1544.
- [10] a) B. C. Stipe, H. J. Mamin, T. D. Stowe, T. W. Kenny, D. Rugar, *Phys. Rev. Lett.* **2001**, 86, 2874; b) B. Gross, D. P. Weber, D. Ruffer, A. Buchter, F. Heimbach, A. Fontcuberta i Morral, D. Grundler, M. Poggio, *Phys. Rev. B* **2016**, 93, 064409; c) J. Jang, D. G. Ferguson, V. Vakaryuk, R. Budakian, S. B. Chung, P. M. Goldbart, Y. Maeno, *Science* **2011**, 331, 186. d) D. P. Weber, D. Ruffer, A. Buchter, F. Xue, E. Russo-Averchi, R. Huber, P. Berberich, J. Arbiol, A. F. I. Morral, D. Grundler, M. Poggio, *Nano Lett.* **2012**, 12, 6139; e) A. Mehlin, F. Xue, D. Liang, H. F. Du, M. J. Stolt, S. Jin, M. L. Tian, M. Poggio, *Nano Lett.* **2015**, 15, 4839.
- [11] A. Franco, F. C. e Silva, *Appl. Phys. Lett.* **2010**, 96, 172505.